ACS APPLIED ENERGY MATERIALS

www.acsaem.org Article

# PdAg Nanoparticles Supported on $Na_2Ti_3O_7$ for $CO_2$ Hydrogenation into Formic Acid: Expanding Catalyst Design from Powder to a Metal 3D-Printed Self-Catalytic Reactor

Naoyuki Hayashida, Hyo-Jin Kim, Kazuki Shun, Hideto Yoshida, Takayoshi Nakano, and Kohsuke Mori*

Cite This: https://doi.org/10.1021/acsaem.6c00086 Read Online

ACCESS | Metrics & More | Article Recommendations | Supporting Information

**ABSTRACT:** Formic acid (FA: HCOOH) has emerged as a promising hydrogen storage material because of its high hydrogen storage density and ease of handling. Thus, a practical and rational heterogeneous catalyst for FA synthesis via liquid-phase $CO_2$ hydrogenation is highly expected. In this study, we first prepared PdAg alloy nanoparticles (NPs) supported on $Na_2Ti_3O_7$ via simple ion-exchange followed by chemical reduction. These powdered specimens promote the efficient selective hydrogenation of $CO_2$ to give FA even under mild reaction conditions. The attack of the dissociated H atom on the $HCO_3^-$ intermediate was found to be the rate-determining step, which is facilitated by PdAg alloy NPs with a low Pd/Ag ratio. The insights obtained from the powdered specimens were subsequently applied to the design of a self-catalytic reactor fabricated using metal three-dimensional (3D)-printing technology. Oxidation and hydrothermal treatment under alkaline conditions of cylindrical-shaped Ti-based catalytic reactors produced $Na_2Ti_3O_7$ nanofibers on their surface, which further enabled the deposition of PdAg NPs via ion-exchange followed by chemical reduction, and facilitated the liquid-phase $CO_2$ hydrogenation into FA. We also investigated the influence of 3D-printing scan strategies on the microstructure and catalytic performance by changing the laser scan direction.

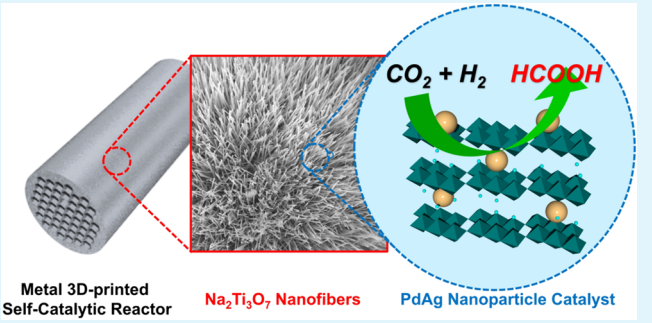


**KEYWORDS:** *PdAg alloy nanoparticles, formic acid, $Na_2Ti_3O_7$, metal 3D-printing, catalytic reactor*



## 1. INTRODUCTION

To realize carbon neutrality, hydrogen ($H_2$) has attracted considerable attention as a next-generation energy vector for solving numerous environmental and energy problems.[1−4] However, its controllable storage and safe transportation remain major challenges.[5−8] Chemical hydrogen storage, which converts hydrogen into stable storage materials through reversible chemical reactions, offers a promising solution. Among various storage materials, formic acid (FA: HCOOH) is considered a promising candidate because of its relatively high hydrogen storage density, high stability, low toxicity, and low flammability.[9−11] In addition, its dehydrogenation can be carried out under mild conditions (20−100 °C), and efficient regeneration via hydrogenation of the $CO_2$ produced during dehydrogenation would enable a sustainable $CO_2$-mediated energy cycle.[12−15]

The gas-phase hydrogenation of $CO_2$ to FA is thermodynamically unfavorable, exhibiting a positive free energy change ($CO_2(g) + H_2(g) \rightarrow HCOOH(l)$ $\Delta G^\circ_{298} = 33$ kJ mol$^{-1}$), whereas the same reaction in aqueous solution proceeds more readily because of its relatively low free energy ($CO_2(aq) + H_2(aq) \rightarrow HCOOH(l)$ $\Delta G^\circ_{298} = -4$ kJ mol$^{-1}$).[16] To make the conversion of $CO_2$ to FA feasible, the thermodynamic equilibrium is shifted toward the positive reaction by adding organic amines or alkali/alkaline-earth bicarbonates ($CO_2(aq) + H_2(aq) + B \rightarrow HCO_3^-(aq) + BH^+$ ($B$: base) $\Delta G^\circ_{298} = -35.4$ kJ mol$^{-1}$).[17] Our group has previously reported that PdAg alloy nanoparticles (NPs) supported on $TiO_2$ exhibit excellent activity in FA synthesis under aqueous basic conditions even when the reaction conditions are relatively mild (100 °C, 2.0 MPa).[18] To achieve an additive-free aqueous process, we recently proposed a heterogeneous tandem catalysis strategy in which $Co_3O_4$ acts as a $CO_2$ hydration cocatalyst to produce a $HCO_3^-$ intermediate, in combination with PdAg/$TiO_2$ as a hydrogenation catalyst of $HCO_3^-$ to produce FA.[19]

Despite this progress, the development of a catalytic reactor that provides optimal reaction conditions is also essential for

Received: January 8, 2026
Revised: March 20, 2026
Accepted: March 24, 2026

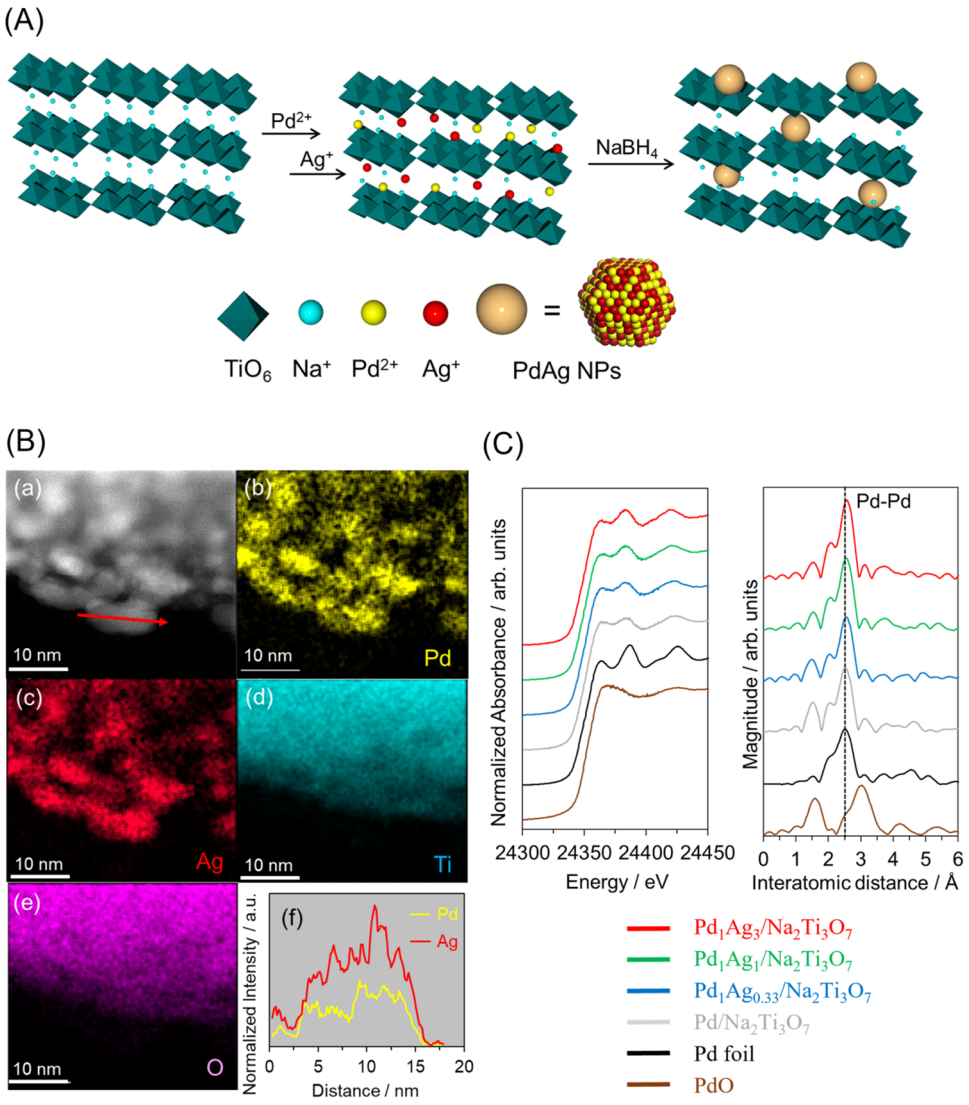


**Figure 1.** (A–C) Structural and electronic characterization of PdAg/$Na_2Ti_3O_7$. (A) Scheme illustrating the preparation process of the catalysts. (B) Morphology and elemental distribution of $Pd_1Ag_3/Na_2Ti_3O_7$: (a) HAADF-STEM image; (b-e) EDS elemental maps of Pd, Ag, Ti, and O; (f) EDS line-scan profile along the analytical direction. (C) Pd K-edge XAS analysis: (a) XANES spectra and (b) FT-EXAFS spectra of the samples.

the practical application of aqueous-phase hydrogenation of $CO_2$ to FA.[20−22] Conventional catalyst development generally involves an initial assessment of a high-performance catalyst with excellent selectivity and reasonable stability, followed by pilot testing and industrial application.[23−25] In this process, research in catalyst and reactor design has traditionally progressed separately; catalyst design mainly focuses on improving inherent properties of catalytic materials, including preparation techniques and reaction mechanisms, whereas reactor studies focus on improving thermal efficiency and reducing pressure drop.[26−28] However, functional integration of catalysts and reactors has been limited; further studies are therefore expected to achieve synergistic effects and more advanced catalyst systems.

Three-dimensional (3D) printing, also known as additive manufacturing (AM), is a promising new technology that addresses the aforementioned issue. In the case of laser powder bed fusion (LPBF), a raw metal powder is first coated onto a build plate in a thin layer using a blade and is selectively melted with a high-intensity laser, resulting in rapid solidification to fabricate two-dimensional (2D) objects. With repeated melting and solidification layer by layer and stacking of 2D objects, the desired 3D object is finally obtained. Unlike conventional cutting processing and casting, metal 3D printing enables the fabrication of catalytic reactors with complex geometries from diverse materials such as alloys and composites,[29−31] offering self-catalytic reactors (SCRs) that integrate catalytic and reactor functions.[32−37] We have developed a multifunctional Ni-based SCR for $CO_2$ methanation by combining metal 3D printing and selective electrochemical dissolution.[38] More interestingly, the LPBF technique enables precise control of material properties, including crystal structure and orientation, which strongly depends on the scan strategy used in the fabrication process.[39−41] Representative scan strategies include the X-scan, in which the laser beam scans repeatedly along the *X*-direction for all layers, and the XY-scan, in which the scanning direction alternates between *X* and *Y* for each successive layer. We successfully enhanced catalytic activity in $CO_2$ methanation by simply switching the scan strategy from X-scan to XY-scan during the fabrication of our Ni-based SCR.[38] Although research on metal 3D-printed catalytic reactors is expanding, the influence of crystal structure and


https://doi.org/10.1021/acsaem.6c00086
ACS Appl. Energy Mater. XXXX, XXX, XXX−XXX

orientation controlled by scan strategy on catalytic performance has been scarcely investigated.[25,38] To address this gap, we systematically investigate this relationship in metal 3D-printed catalytic reactors.

Our final objective in the present study is to develop an SCR for FA synthesis via liquid-phase $CO_2$ hydrogenation. As a preliminary step, PdAg alloy NPs were supported on powdered $Na_2Ti_3O_7$ via an ion-exchange method, followed by reduction using sodium borohydride ($NaBH_4$), to evaluate the promising properties of $Na_2Ti_3O_7$ as a support material. This investigation revealed that PdAg alloy NPs with a low Pd/Ag ratio efficiently catalyze $CO_2$ hydrogenation into FA and that the attack of the dissociated H atom on the $HCO_3^-$ intermediate is the rate-determining step of the overall catalytic cycle. Building on the insights obtained from the powder catalyst system, we applied this catalyst design concept to a 3D-printed Ti-based catalytic reactor by forming $Na_2Ti_3O_7$ nanofibers on its surface via oxidation and hydrothermal treatment under alkaline conditions. We further examined how scan strategies influence the structural properties of the SCR and its catalytic performance in FA synthesis.

## 2. RESULTS AND DISCUSSION

Supported PdAg catalysts were prepared by subsequent ion-exchange of $Na_2Ti_3O_7$ using $H_2PdCl_4$ and $AgNO_3$, followed by chemical reduction using $NaBH_4$ in alkaline solution (Figure 1A). The Pd/Ag atomic ratio in the synthesized catalysts was systematically controlled by varying the Ag precursor concentration while maintaining a constant Pd loading of 1.0 wt %. Figure S1A shows the X-ray diffraction (XRD) patterns of PdAg-supported $Na_2Ti_3O_7$ with different Pd/Ag ratios, together with the pattern of the original $Na_2Ti_3O_7$. The patterns of all of the samples show strong diffraction peaks at approximately 10.5°, 25.7°, 43.8°, and 48.5°, which are attributed to the $Na_2Ti_3O_7$. In particular, the diffraction peak around 25.7° slightly shifted toward a higher angle after PdAg loading, which suggests that Pd and Ag ions initially introduced via the ion-exchange process migrated from the interlayer and formed PdAg NPs on the external surface during the subsequent reduction step (Figure S1B). Although the diffraction intensity of $Na_2Ti_3O_7$ decreased slightly after the metals were loaded, the layered structure was largely maintained without substantial deterioration of crystallinity. In addition, only the patterns of the metal−supported samples show weak diffraction peaks at approximately 11.2° and 24.4°, which correspond to $H_2Ti_3O_7$.[42] Proton exchange of $Na_2Ti_3O_7$ is known to be energetically favorable, and its composition is easily changed to $Na_{2-x}H_xTi_3O_7$.[43] Given that the pH of the filtrate after ion exchange was approximately 10, we inferred that these samples underwent proton exchange. These results indicate that the introduction of metals does not cause substantial structural changes in the support material. In addition, no peaks corresponding to Pd or Ag were observed because of their low loading and high dispersion.

Transmission electron microscopy (TEM) analysis showed that both Pd and PdAg NPs were uniformly and highly dispersed on the $Na_2Ti_3O_7$ support (Figures S2−S5). The average particle sizes evaluated from TEM images were 7.3, 5.5, 5.0, and 6.1 nm for $Pd/Na_2Ti_3O_7$, $Pd_1Ag_{0.33}/Na_2Ti_3O_7$, $Pd_1Ag_1/Na_2Ti_3O_7$, and $Pd_1Ag_3/Na_2Ti_3O_7$, respectively. These observations indicate that alloying Pd with Ag resulted in a slight reduction in particle size, thereby increasing the number of exposed active sites on the catalyst surface. High-angle annular dark field scanning transmission electron microscopy (HAADF-STEM) images together with energy-dispersive X-ray spectroscopy (EDS) elemental mapping further confirmed the high dispersion of Pd and PdAg NPs (Figures S6 and 1B(a−f)). EDS line-scan analysis demonstrated that Pd and Ag species were distributed in the same regions within individual NPs, suggesting the successful formation of PdAg alloy NPs (Figure 1B(f)).

X-ray absorption spectroscopy (XAS) was used to clarify the oxidation state and local structure of Pd in the Pd and PdAg catalysts. The normalized Pd K-edge X-ray absorption near edge structure (XANES) spectra of the PdAg catalysts closely resembles those of Pd foil and the monometallic Pd catalyst, whereas they are clearly distinct from that of PdO (Figure 1C(a)). These observations indicate that the Pd species in both the PdAg and monometallic Pd catalysts are in a metallic state. In addition to the spectral features, the absorption edge energies (measured at the half-height of the normalized edge jump) corresponding to different Pd/Ag ratios are summarized in Table S1. The edge position depends on the electronic charge of the Pd species, and the energy decreased in the order Pd (24349.6 eV) > $Pd_1Ag_{0.33}$ (24349.4 eV) > $Pd_1Ag_1$ (24349.1 eV) > $Pd_1Ag_3$ (24348.9 eV). These results indicate that the Pd atoms in the PdAg NPs are in an electron-rich state due to charge transfer from the Ag atoms, which occurs because of the net difference in ionization potential between the Pd (8.34 eV) and Ag (7.57 eV); substantial electron enrichment of the Pd species was therefore observed with increasing Ag loading amount.

The Fourier transform extended X-ray absorption fine structure (FT-EXAFS) spectra at the Pd K-edge show a single, well-defined peak at approximately 2.5 Å, which corresponds to Pd−Pd coordination (Figure 1C(b)). The spectrum of the PdO reference shows characteristic Pd−O and Pd−O−Pd peaks at ∼1.6 and ∼3.0 Å, respectively, whereas no such oxygen-related peaks are observed for the Pd or PdAg catalysts. These results indicate that the Pd species are in a metallic state. In addition, the Pd−Pd distance in the PdAg catalysts are slightly longer than those in the Pd foil and in the monometallic Pd catalyst, suggesting PdAg alloy formation. The formation of PdAg alloy was evaluated based on the changes in the interatomic distances in this study, since Pd and Ag are adjacent elements in the periodic table and exhibit very similar backscattering properties.[44] Because Pd and Ag ions are completely solid-solubilized and have similar reduction potentials ($E^0(Pd^{2+}/Pd^0)$ = +0.99 V, $E^0(Ag^+/Ag^0)$ = +0.80 V), PdAg alloy NPs with a random structure can be easily formed by coreduction of Pd and Ag precursors. As shown in Figure S7, the Ag K-edge XANES spectra of the PdAg catalysts are similar to those of Ag foil and the monometallic Ag catalyst while exhibiting spectral features that differ from those of the $Ag_2O$ reference. These observations suggest that the Ag in both the PdAg and monometallic Ag catalysts is predominantly in a reduced state. The Ag K-edge FT-EXAFS spectra (Figure S8) show a distinct peak at approximately 2.7 Å, characteristic of metallic Ag−Ag coordination, which further confirms the presence of metallic Ag in the PdAg catalysts. Notably, the Ag−Ag bond distance in the PdAg catalysts is shorter than that in the Ag foil. This contraction results from the incorporation of Pd, whose smaller atomic radius reduces the local Ag−Ag bond distances. When considered in combination with the Pd-side coordination changes, these findings consistently indicate the formation of a PdAg alloy.


https://doi.org/10.1021/acsaem.6c00086
ACS Appl. Energy Mater. XXXX, XXX, XXX−XXX

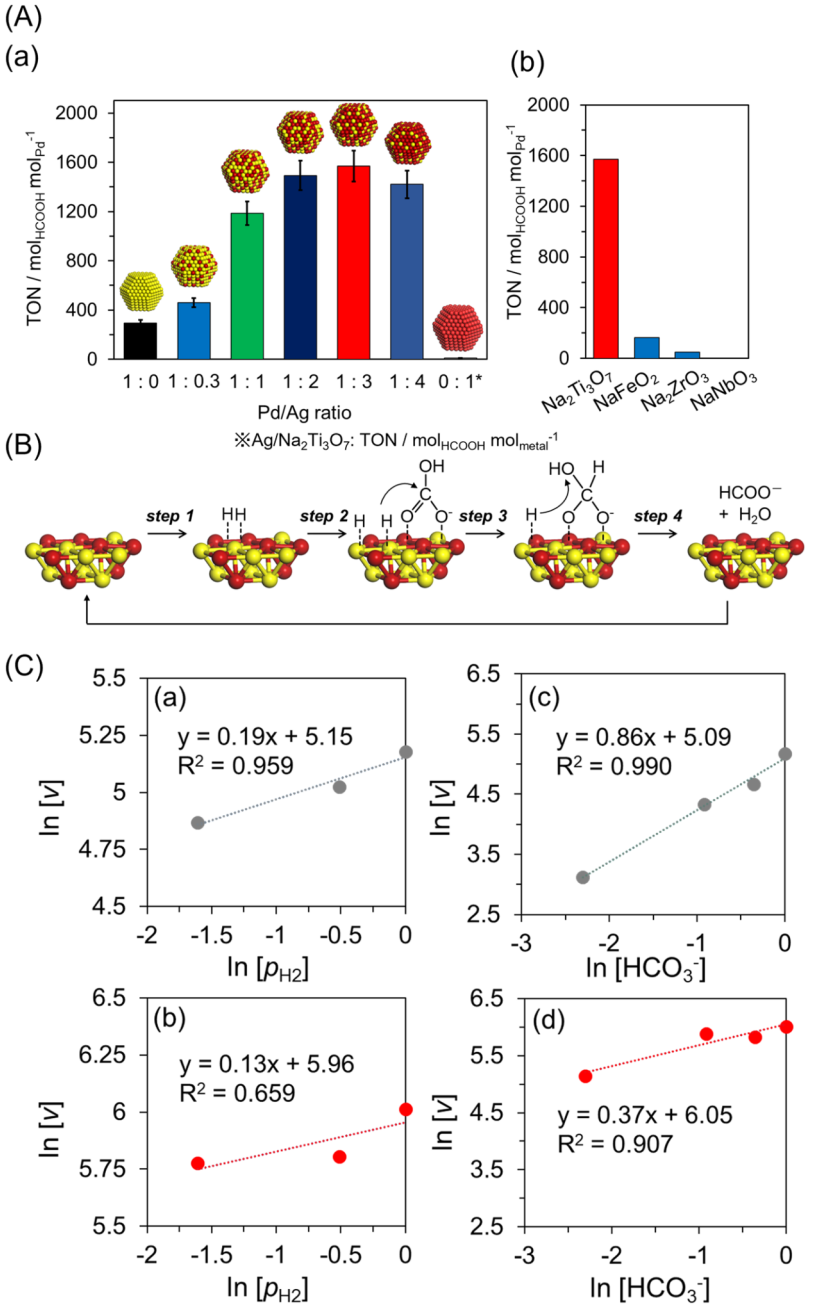


**Figure 2.** (A–C) Catalytic performance and kinetic analysis of PdAg/$Na_2Ti_3O_7$ catalysts. (A) (a) Effect of Pd/Ag ratio on the TON values for PdAg/$Na_2Ti_3O_7$ catalysts; (b) effect of layered oxide supports on the TON values of $Pd_1Ag_3$ catalysts. (B) Scheme of the proposed reaction mechanism over PdAg/$Na_2Ti_3O_7$. (C) Kinetic analysis: (a, b) plots of ln $k$ versus ln $P_{H2}$ for Pd/$Na_2Ti_3O_7$ and $Pd_1Ag_3$/$Na_2Ti_3O_7$, respectively; (c, d) plots of ln $v$ versus ln [$HCO_3^-$] for Pd/$Na_2Ti_3O_7$ and $Pd_1Ag_3$/$Na_2Ti_3O_7$, respectively.

The catalytic performance in the hydrogenation of $CO_2$ into FA showed a strong dependence on the Pd/Ag ratio. The TON values normalized to the amount of Pd after 24 h varied substantially with the Ag content: monometallic Pd/$Na_2Ti_3O_7$ exhibited only moderate activity (TON = 295, TOF = 12.3), whereas the reaction using monometallic Ag/$Na_2Ti_3O_7$ hardly occurred (Figure 2A(a)). The TON values increased progressively with increasing Ag loading, reaching a maximum at a Pd:Ag atomic ratio of 1:3 (TON = 1569, TOF = 65.4), beyond which the activity decreased. The maximum TON value represents a more than 5-fold increase over that of the TON value of the monometallic Pd/catalyst. Notably, the present catalyst exhibited an activity comparable to that of our previously reported PdAg/$TiO_2$ catalyst.[18] The observed composition-dependent behavior suggests that high activity arises from the formation of homogeneous PdAg alloy NPs on the $Na_2Ti_3O_7$ surface and the resultant synergistic interaction between Pd and Ag. In particular, given that no substantial differences in the average NPs diameters were observed by TEM analysis, the superior activity of Ag-rich catalysts suggests that factors other than particle size govern the catalytic performance. As we previously reported, geometrically isolated and electron-rich active Pd species exhibit superior activity for FA synthesis, and a similar electronic and geometric effect is likely responsible for the enhanced catalytic activity.[18] To evaluate the support capability of $Na_2Ti_3O_7$, we compared its


https://doi.org/10.1021/acsaem.6c00086
ACS Appl. Energy Mater. XXXX, XXX, XXX−XXX

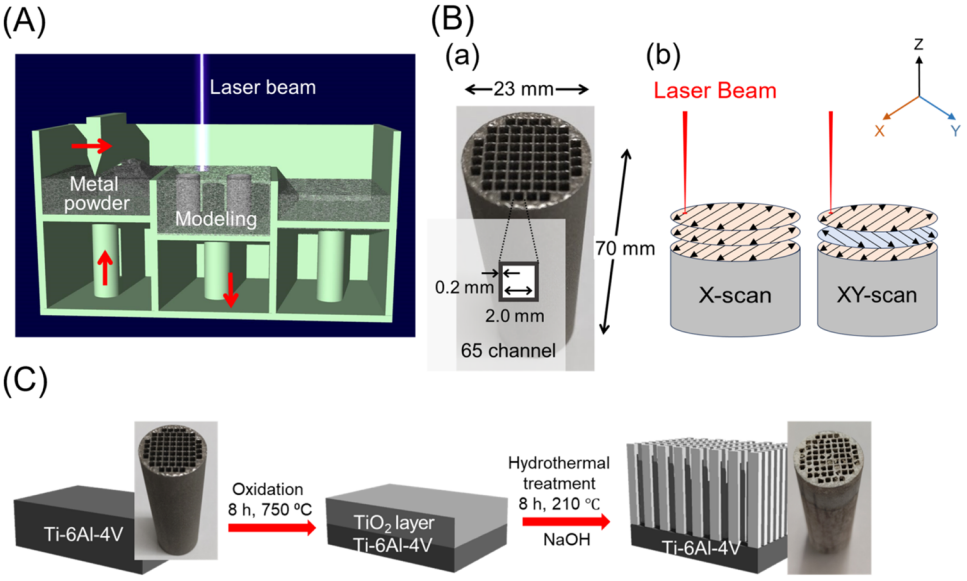


**Figure 3.** (A–C) SCR fabrication schemes. (A) Scheme of the reactor formation process by L-PBF. (B) (a) Structure and dimensions of the Ti-6Al-4 V reactor fabricated by 3D printing; (b) scheme of the X-scan and XY-scan strategies. (C) Scheme of the SCR fabrication procedure.

catalytic performance with those of several oxide supports. $Na_2MoO_4$ readily dissolved in water and therefore could not function as a stable support, and the catalysts supported on $NaFeO_2$, $Na_2ZrO_3$, and $NaNbO_3$ exhibited substantially lower catalytic activities than that supported on $Na_2Ti_3O_7$ (Figure 2A(b)). These results indicate that $Na_2Ti_3O_7$ provides superior support characteristics relative to the other oxide materials examined.

On the basis of previous experimental and theoretical investigations into the reaction mechanisms of metal NPs, we propose a possible catalytic cycle for $CO_2$ hydrogenation into FA over supported PdAg NPs (Figure 2B).[45−47] According to our previous DFT calculations, $H_2$ dissociation preferentially occurs on Pd sites rather than Ag sites due to the substantially lower dissociation energy barrier on Pd sites.[18] Therefore, we propose that the reaction initiates with the dissociative activation of $H_2$ on Pd sites, generating surface metal-hydride species (step 1). Previous mechanistic studies on Pd catalysts have identified bicarbonate species as key intermediates in liquid-phase $CO_2$ hydrogenation. Based on these findings, $HCO_3^-$ formed under basic conditions is proposed to adsorb onto PdAg NPs (step 2), where it is hydrogenated to produce a formate intermediate (step 3). Thermodynamically, the reduction of $HCO_3^-$ is more favorable when the active hydrogen species attack the carbon atom rather than the oxygen atoms.[48] Finally, the formation of formate, accompanied by the generation of $H_2O$, regenerates the initial active sites and completes the catalytic cycle (step 4). Our previous DFT calculation results indicate that the elementary steps involving $HCO_3^-$ species (step 2 and step 3) represent the rate-determining process, rather than those associated with hydrogen species (step 1 and step 3).[18] The catalytic activity exhibited only a slight dependence on the $H_2$ partial pressure upon Ag incorporation (Figure 2C(a,b)). The corresponding reaction orders were 0.19 for $Pd/Na_2Ti_3O_7$ and 0.13 for $Pd_1Ag_3/Na_2Ti_3O_7$, indicating that the Ag addition does not facilitate the elementary step involving hydrogen species (step 1 or step 3). By contrast, the dependence of the catalytic activity on the $HCO_3^-$ concentration was strongly influenced by Ag incorporation (Figure 2C(c,d)). The corresponding reaction orders were 0.86 for $Pd/Na_2Ti_3O_7$ and 0.37 for $Pd_1Ag_3/Na_2Ti_3O_7$, suggesting that the addition of Ag substantially enhances the rate-determining step associated with $HCO_3^-$ species (step 2 or step 3). Such an enhancement of the rate-determining step by the PdAg alloy NPs with a low Pd/Ag ratio can be explained by an electronic ligand effect resulting from the interplay between active Pd atoms and neighboring Ag atoms; the negatively charged Pd atom accordingly decreases the electronegativity of the dissociated hydride species.[49] By contrast, the $HCO_3^-$ species favorably adsorbs onto the positively charged Ag atom. Therefore, electronically promoted hydride species preferentially attack the carbon atoms of the adsorbed $HCO_3^-$ by electronic interaction. While the above discussion focuses on the electronic effects of the PdAg alloy nanoparticles, the possible contribution of the $Na_2Ti_3O_7$ support to $HCO_3^-$ stabilization was also examined. To examine the potential role of the $Na_2Ti_3O_7$ support in stabilizing $HCO_3^-$ species, a preliminary adsorption experiment was conducted. The calculated adsorption amount was negligible, indicating that direct $HCO_3^-$ adsorption on the $Na_2Ti_3O_7$ support is not a dominant contributor to the catalytic cycle.

Cylindrical-shaped catalytic reactors with a diameter of 14 mm and length of 40 mm were fabricated by LPBF using Ti-6Al-4 V powder as a starting material (Figure 3A). To elucidate the effect of the scan strategy, we fabricated the catalytic reactors using two scan modes: the X-scan, in which the laser beam scans repeatedly along the *X*-direction for all layers, and the XY-scan, in which the scanning direction alternates between *X* and *Y* for each successive layer (Figure 3B). The obtained Ti-based reactor was subsequently oxidized at 750 °C for 8 h to form a $TiO_2$ layer on its surface, which was further subjected to hydrothermal treatment at 210 °C for 8 h under alkaline conditions to generate $Na_2Ti_3O_7$ nanofibers according to the eq $3TiO_2 + 2NaOH \rightarrow Na_2Ti_3O_7{\cdot}H_2O$ (Figure 3C). Pd and Ag precursors were easily deposited onto the $Na_2Ti_3O_7$ nanofibers using a simple ion-exchange procedure, similar to the deposition of Pd and Ag onto the


https://doi.org/10.1021/acsaem.6c00086
ACS Appl. Energy Mater. XXXX, XXX, XXX−XXX

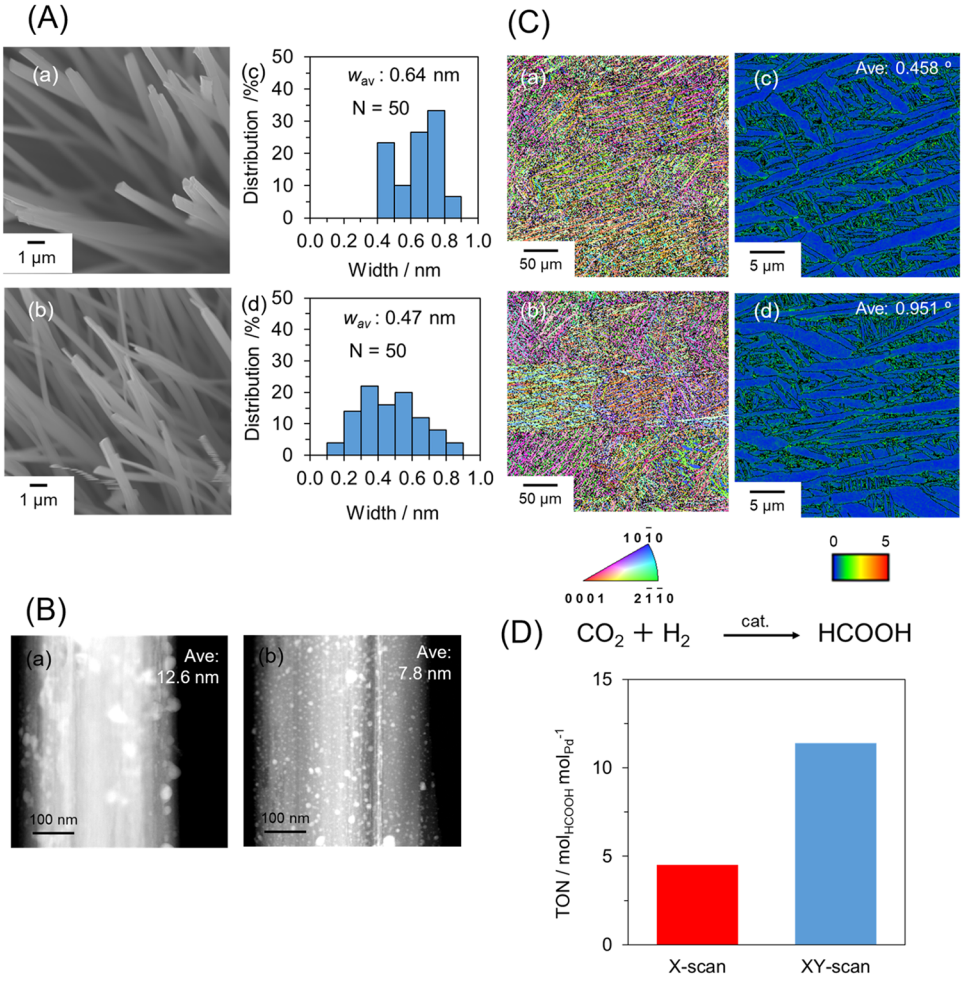


**Figure 4.** (A–D) Microstructural characterization and catalytic performance of SCRs fabricated using X-scan and XY-scan strategies. (A) (a, b) SEM images of $Na_xTi_yO_z$ nanofibers grown on Ti-6Al-4 V substrates fabricated by X-scan and XY-scan, respectively; (c, d) histograms of the nanofiber diameter distributions for the samples fabricated by X-scan and XY-scan, respectively. (B) (a, b) HAADF-STEM images of PdAg alloy NPs supported on $Na_xTi_yO_z$ grown on Ti-6Al-4 V substrates fabricated by (a) X-scan and (b) XY-scan. (C) (a, b) IPF maps of Ti-6Al-4 V substrates fabricated by (a) X-scan and (b) XY-scan; (c, d) KAM maps of Ti-6Al-4 V substrates fabricated by (c) X-scan and (d) XY-scan. (D) Catalytic activity of SCRs fabricated using each scan strategy.

powdered sample, and PdAg NPs were subsequently generated by reduction with aqueous $NaBH_4$ solution, yielding an SCR. The Pd loading of each reactor was determined by inductively coupled plasma atomic emission spectroscopy (ICP-AES) analysis of the Pd precursor solution after it had passed through the reactor (Table S2). For surface characterization, the same treatment was also carried out on plate-shaped samples. The corresponding plane in the reactor is depicted in Figure S9.

The XRD patterns of the $Na_xTi_yO_z$ nanofibers grown on Ti–6Al–4 V substrates are presented in Figure S10. In both samples, diffraction peaks attributable to $Na_2Ti_3O_7$ are observed at approximately 11° and 28°, along with a peak corresponding to $Na_2Ti_7O_{15}$ near 45°, confirming the formation of $Na_xTi_yO_z$ nanofibers.[42,50] A reflection at ∼36° was further assigned to $H_2Ti_3O_7$, which is considered to form through proton exchange during the hydrothermal process.[42] Notably, no substantial differences in the crystalline phases were identified between the two scan strategies. SEM observation revealed the formation of nanofiber structures (Figure 4A(a,b)). The elemental composition of the nanofibers was analyzed by EDS, which confirmed the presence of Na, Ti, and O, consistent with the formation of $Na_xTi_yO_z$ (Figures S11 and S12). The nanofiber size distribution histograms indicate that average diameter obtained with the XY-scan strategy is 0.47 μm, which is a smaller and broader distribution than that obtained with the X-scan strategy, which produces nanofibers with an average diameter of 0.64 μm (Figure 4A(c,d)). The HAADF-STEM images acquired after the metals were loaded clearly indicate the formation of highly dispersed PdAg NPs with a mean diameter of 7.8 nm and a narrow size distribution on the nanofiber surface obtained by XY-scan (Figures 4B(b) and S13(b)). By contrast, larger NPs with a mean diameter of 12.6 nm are observed on the nanofiber surface obtained by X-scan (Figures 4B(a) and S13(a)). These results indicate that the scan strategy strongly influences not only on the diameter of the $Na_2Ti_3O_7$ nanofibers but also the distribution and particle size of the supported NPs.

To elucidate the effect of the scan strategy, we analyzed the as-fabricated specimen by electron backscatter diffraction (EBSD). In the SEM images, both specimens exhibit a fine acicular α' martensitic microstructure with features spaced approximately 100 μm apart, which is typically observed in Ti-6Al-4 V alloys fabricated by the LPBF process (Figure S14).


https://doi.org/10.1021/acsaem.6c00086
ACS Appl. Energy Mater. XXXX, XXX, XXX–XXX

The inverse pole figure (IPF) maps show differences between the two scan strategies. The specimen fabricated by X-scan exhibited a relatively uniform color distribution, indicating locally similar crystallographic orientations (Figure 4C(a)). By contrast, the XY-scan specimen showed a slightly more heterogeneous distribution, suggesting that the crystal orientation was not uniformly aligned (Figure 4C(b)). These results indicate that, compared with the XY-scan, the X-scan tends to produce microstructures with more uniformly aligned crystal orientations. The kernel average misorientation (KAM) value, defined as the average misorientation between a measurement point and its six nearest neighboring points, is a commonly used scalar parameter that provides an approximate characterization of dislocation in EBSD analysis.[51−53] The average KAM values of the X-scan and XY-scan specimens were 0.458° and 0.951°, respectively (Figure 4C(c,d)). The dislocation density, defined as the total dislocation length per unit volume, can be divided into two components: statistically stored dislocation (SSD), which represents uniform plastic deformation, and geometrically necessary dislocations (GNDs), which correspond to the distortion of the crystal lattice introduced by plastic deformation. The GND density can be estimated from the KAM value using the relationship[54]

$$\mathrm{GND} = 2(\mathrm{KAM\ value})/(b \times L)$$

where $b$ is the magnitude of the Burgers vector and $L$ is the measurement step size. On the basis of this relationship, the XY-scan specimen is suggested to possess a higher dislocation density than the X-scan substrate.

On the basis of previous studies, we propose the following formation mechanism for $Na_2Ti_3O_7$ nanofibers (Figure S15).[55] Initially, $TiO_2$ layers form on the substrate surface during the oxidation process. Because of the mismatch in thermal expansion coefficients between the oxide layer and the substrate, cracks are generated within the oxide layer. The high-concentration NaOH solution then partially dissolves the $TiO_2$ layer, generating unstable Ti ionic species. These Ti ionic species subsequently crystallize, leading to the formation of $Na_2Ti_3O_7$ nanofibers on the surface. Nucleation is known to preferentially occur at crystal defects, such as dislocations and grain boundaries. Among these defects, grain boundaries are generally more favorable nucleation sites than dislocations. Similarly, $Na_2Ti_3O_7$ nanofibers can nucleate at these defect sites. Nucleation may occur not only at grain boundaries but also along dislocations on the XY-scan substrate, which has a higher dislocation density. This tendency could account for the broader dispersion in nanofiber diameters observed for the XY-scan substrate compared with the X-scan substrate.

We subsequently evaluated the catalytic activity of the SCRs under reaction conditions similar to those used for the powdered catalysts, except for the total pressure and solvent volume. Both SCRs exhibited clear activity toward the hydrogenation of $CO_2$ into FA (Figure 4D). Notably, the SCR fabricated using the XY-scan strategy exhibited higher activity than that fabricated using the X-scan strategy, which we attributed to a higher density of small PdAg NPs supported on the nanofiber surface. In addition, the highly active SCR fabricated with the XY-scan strategy was applied to the flow reaction system in the hydrogenation of $NaHCO_3$ to formate ($NaHCO_3 + H_2 \rightarrow HCOONa + H_2O$). Formate generation was confirmed under continuous supply of pressured $H_2$ and aqueous $NaHCO_3$, with a TON of 46, indicating that the SCR effectively functions even under flow-reactor conditions (Figure S16 and Table S3). We speculate that a greater enhancement of the activity could be achieved by screening the reaction condition details. Further experiments are now underway in our laboratory.

## 3. CONCLUSION

We developed an efficient catalyst for the hydrogenation of $CO_2$ into FA. Initially, PdAg alloy NPs were supported on powdered $Na_2Ti_3O_7$, and structural and electronic modifications associated with PdAg alloying were found to have contributed to the enhanced catalytic performance. The Ag-rich Pd/Ag = 1:3 catalyst exhibited the highest activity among the investigated samples. The insights obtained from the powder catalysts were subsequently applied to SCRs. Differences in the laser scanning direction resulted in changes in surface microstructures, nanofiber morphology, and metal dispersion states, which were accompanied by corresponding differences in catalytic activity. These findings indicate that the scanning strategy has the potential to control the structural and functional properties of SCRs. Overall, this study demonstrates the effectiveness of using metal 3D-printing technology for catalytic reactor design and provides new perspectives for future developments in reaction engineering and catalyst materials.

## 4. EXPERIMENTAL SECTION

### 4.1. Materials

$Na_2Ti_3O_7$ was obtained from Kojundo Chemical Laboratory. HCl, NaOH, $PdCl_2$, $AgNO_3$, $NaBH_4$, and $NaHCO_3$ were purchased from Nacalai Tesque. All commercially available reagents were used as received. Distilled water was used as the reaction solvent.

### 4.2. Catalyst Synthesis

An aqueous HCl solution (150 mL, pH 2) containing $PdCl_2$ (0.189 mmol) was stirred for 15 min to ensure complete dispersion of the Pd precursor. $Na_2Ti_3O_7$ (2.00 g) was then added, and the resultant mixture was stirred at room temperature for 2 h to allow $Pd^{2+}$ ions to be exchanged onto the support. The solid was collected by vacuum filtration and dried under reduced pressure to obtain $Pd^{2+}/Na_2Ti_3O_7$. Distilled water (50 mL), $Pd^{2+}/Na_2Ti_3O_7$ (0.500 g), and $AgNO_3$ (0.047 mmol) were subsequently mixed and stirred at room temperature for 2 h to introduce Ag. To ensure uniform reduction, a NaOH aqueous solution (0.0055 mmol) was added to adjust the pH to approximately 10, and the resultant mixture was stirred at room temperature for an additional 30 min. Dissolved $O_2$ was removed by Ar bubbling at room temperature for 20 min. $NaBH_4$ (0.938 mmol, corresponding to ten times the total molar amount of the added metals) was subsequently added to the mixture under stirring at room temperature to reduce the metal precursors, and the suspension was stirred for 30 min to complete the reduction. The obtained catalyst was collected by vacuum filtration and dried under reduced pressure. As a result, $Pd_1Ag_1/Na_2Ti_3O_7$ (Pd: 1.0 wt %, Pd/Ag molar ratio = 1/1) was obtained. Additional samples were prepared by systematically varying the Pd/Ag molar ratio while keeping the Pd loading constant.

### 4.3. Fabrication of the SCR

Ti-6Al-4 V powder (Sanyo Special Steel, Hyogo, Japan) produced by gas atomization was used as the starting material. The specimens were fabricated by LPBF using an EOS M 290 system (EOS, Krailling, Germany). Three types of components were fabricated using either an X-scan or an XY-scan strategy: a Ti-6Al-4 V substrate and two cylinder-shaped reactors with dimensions of 23 mm × 70 mm and 14 mm × 40 mm; the 23 mm reactor was produced using either the X-scan or XY-scan strategy, whereas the 14 mm reactor was fabricated using only the XY-scan strategy. During fabrication, the build platform was heated to 80 °C, and the $O_2$ concentration was maintained below


https://doi.org/10.1021/acsaem.6c00086
ACS Appl. Energy Mater. XXXX, XXX, XXX−XXX

100 ppm by purging with Ar gas. The laser power ($P$), scan speed ($v$), hatch distance ($d$), and layer thickness ($t$) were set to 250 W, 1200 mm $s^{-1}$, 0.1 mm, and 0.06 mm, respectively.

The as-printed Ti-6Al-4 V AM reactor was sonicated in acetone for 15 min and subsequently dried in an oven at 100 °C for 1 h. The Ti-6Al-4 V AM reactor was then oxidized in a furnace at 750 °C for 8 h with a ramp of 5 °C $min^{-1}$. The oxidized Ti-6Al-4 V AM reactor was placed at the center of a Teflon rack inside a Teflon-lined stainless-steel autoclave filled with 300 mL of 10 M NaOH and sealed. The autoclave was then heated in an oven at a ramp rate of 5 °C $min^{-1}$ to 210 °C and held at this temperature for 8 h to complete the hydrothermal treatment. The resultant $Na_xH_{2-x}Ti_3O_7$/Ti-6Al-4 V AM reactor was washed with deionized water until the pH of the filtrate reached ∼10 and was subsequently dried at 100 °C overnight. The same hydrothermal procedure was applied to the Ti-6Al-4 V substrate, except that 40 g of 10 M NaOH was used instead of 300 mL of 10 M NaOH. In the ion-exchange process, 200 mL of a 5 mM $PdCl_2$ solution in 0.01 M HCl was circulated through the $Na_2Ti_3O_7$/Ti-6Al-4 V AM reactor at a flow rate of 22 mL $min^{-1}$ at room temperature for 3 h. After the $PdCl_2$ solution had circulated, the reactor was removed and dried under vacuum. Once the reactor was sufficiently dried, 200 mL of a 15 mM $AgNO_3$ aqueous solution was circulated through the reactor under the same flow conditions as the $PdCl_2$ solution, followed by vacuum drying. For the reduction step, 200 mL of an aqueous $NaBH_4$ solution containing 151.3 mg of $NaBH_4$ (equivalent to the total moles of the introduced metals) was circulated through the reactor at 22 mL $min^{-1}$ at room temperature for 5 min. The reactor was then removed and dried under vacuum to obtain the reduced PdAg/$Na_2Ti_3O_7$/Ti-6Al-4 V AM reactor (SCR). For the smaller reactor, the procedure was the same except that precursor solutions with different concentrations were used ($PdCl_2$: 0.05 mM; $AgNO_3$: 0.15 mM).

### 4.4. Reaction Conditions

$CO_2$ hydrogenation to FA using powdered catalysts was carried out in a batch reactor system equipped with a 60 mL stainless steel autoclave. In each run, the catalyst (10 mg) and an aqueous $NaHCO_3$ solution (1.0 M, 15 mL) were charged into the reactor and the internal pressure was adjusted to 2.0 MPa by introducing a $H_2/CO_2$ mixture (1:1). The reactor was then heated to 100 °C and maintained at this temperature under stirring for 24 h. For catalytic tests using the catalytic AM reactor, $CO_2$ hydrogenation was conducted under the same conditions as described above, except that an autoclave with an internal volume of 125 mL was used, the volume of the 1.0 M $NaHCO_3$ solution was adjusted to 40 mL, and the total pressure was changed to 1.5 MPa. $CO_2$ hydrogenation was also evaluated under continuous-flow conditions using the catalytic AM reactor. The reaction was conducted with a column-type flow reactor (FFX-1000G, EYELA). The reactor was heated to 80 °C, and the effluent was collected after 2 h. $H_2$ was supplied at 10 mL $min^{-1}$, and a 1.0 M aqueous $NaHCO_3$ solution was introduced at 0.50 mL $min^{-1}$. FA yields were quantified by high-performance liquid chromatography (HPLC) using a Shimadzu system equipped with a Bio-Rad Aminex HPX-87H ion-exclusion column (300 × 7.8 $mm^2$). The mobile phase consisted of 5 mM $H_2SO_4$ at flow rate of 0.5 mL $min^{-1}$, with the column temperature maintained at 40 °C. Turnover number (TON) values were calculated by dividing the amount of FA produced after 24 h by the moles of total Pd in the catalyst. For Ag/$Na_2Ti_3O_7$, TON values were calculated using the total moles of the added metal.

### 4.5. Characterization

XRD patterns were recorded using a Rigaku Ultima IV diffractometer equipped with a Cu K$\alpha$ radiation source ($\lambda$ = 1.54056 Å). TEM images were obtained using a Hitachi HF-2000 field-emission transmission electron microscope operated at 200 kV. Particle size distributions were obtained from multiple TEM images acquired from different regions, based on measurements of 100 nanoparticles per sample. STEM images and elemental maps were acquired using a JEOL ARM-200F microscope equipped with a Kvex EDS detector (JED-2300T) operated at 200 kV. Pd and Ag K-edge X-ray absorption fine structure (XAFS) spectra were recorded in fluorescence mode at the BL01B1 beamline of the Spring-8 synchrotron facility (JASRI, Harima, Japan; proposal no. 2024B1566 and 2025A1703) using a Si(111) monochromator. Data processing was performed using the REX2000 software (Rigaku). Fourier transforms of the $k^3$-weighted extended X-ray absorption fine structure (EXAFS) spectra were acquired over the $k$-range 3.0−12.6 $Å^{-1}$ to obtain radial structure functions. The $HCO_3^-$ adsorption experiment was performed as follows. $Na_2Ti_3O_7$ (50 mg) was added to the 0.06 M $NaHCO_3$ aqueous solution (50 mL) and stirred at room temperature. After 2 h, the $Na_2Ti_3O_7$ was removed by filtration and the 0.03 M methylorange aqueous solution (20 $\mu$L) as an acid−base indicator was added to the filtrate (2.5 mL). The amount of adsorbed $HCO_3^-$ was determined by the neutralization titration using 0.1 M HCl aqueous solution as a standard solution. The adsorption amount was calculated from the difference in $HCO_3^-$ concentration before and after contact with $NaHCO_3$. Scanning electron microscopy (SEM) and EDS analyses were carried out using a JSM-6500F microscope (JEOL, Tokyo, Japan) equipped with an Ultima Max EDS detector (Oxford Instruments, Abingdon-on-Thames, UK). Nanofiber diameter distributions were obtained from SEM images, based on measurements of 50 nanofibers per sample. Crystal textures were examined by EBSD using a Hikari high-speed EBSD detector (TSL Solutions) operated at an accelerating voltage of 20 kV. EBSD measurements were conducted with a step size of 0.05 $\mu$m over scan areas of 25 $\mu$m × 25 and 500 $\mu$m × 500 $\mu$m. The diffraction patterns were processed using OIM Analysis software (version 8.6). Metal concentrations were determined by ICP-AES using a Nippon Jarrell-Ash ICAP-575 Mark II spectrometer.

## ■ ASSOCIATED CONTENT

### Supporting Information

The Supporting Information is available free of charge at https://pubs.acs.org/doi/10.1021/acsaem.6c00086.

Additional data for XRD, TEM, STEM, XAS, SEM, EDS, EBSD, ICP-AES, and catalytic performance tests (PDF)

## ■ AUTHOR INFORMATION


### Corresponding Author

**Kohsuke Mori** − *Division of Materials and Manufacturing Science, Graduate School of Engineering, The University of Osaka, Suita, Osaka 565-0871, Japan; Anisotropic Design & Additive Manufacturing Science, Graduate School of Engineering, The University of Osaka, Suita, Osaka 565-0871, Japan; Innovative Catalysis Science Division, Institute for Open and Transdisciplinary Research Initiatives (ICS-OTRI), The University of Osaka, Suita, Osaka 565-0871, Japan;* orcid.org/0000-0003-3915-4528; Phone: +81-6-6879-7460; Email: mori@mat.eng.osaka-u.ac.jp; Fax: +81-6-6105-5029

### Authors

**Naoyuki Hayashida** − *Division of Materials and Manufacturing Science, Graduate School of Engineering, The University of Osaka, Suita, Osaka 565-0871, Japan*

**Hyo-Jin Kim** − *Division of Materials and Manufacturing Science, Graduate School of Engineering, The University of Osaka, Suita, Osaka 565-0871, Japan*

**Kazuki Shun** − *Division of Materials and Manufacturing Science, Graduate School of Engineering, The University of Osaka, Suita, Osaka 565-0871, Japan;* orcid.org/0009-0005-3669-8513

**Hideto Yoshida** − *SANKEN, The University of Osaka, Ibaraki, Osaka 567-0047, Japan*




https://doi.org/10.1021/acsaem.6c00086
ACS Appl. Energy Mater. XXXX, XXX, XXX−XXX

**Takayoshi Nakano** − *Division of Materials and Manufacturing Science, Graduate School of Engineering, The University of Osaka, Suita, Osaka 565-0871, Japan; Anisotropic Design & Additive Manufacturing Science, Graduate School of Engineering, The University of Osaka, Suita, Osaka 565-0871, Japan*

Complete contact information is available at: https://pubs.acs.org/10.1021/acsaem.6c00086

### Author Contributions

N.H. and K.M. conceived the outline of the manuscript. N.H. performed sample preparation, evaluation, characterization and wrote the original draft of the manuscript. H.K. and T.N. helped with the fabrication and evaluation of the SCR. K.S. helped with the measurement of the XAFS data. H.Y. performed STEM observation. K.M. supervised the project and helped with writing the manuscript. All authors have given approval to the final version of manuscript.

### Notes

The authors declare no competing financial interest.

## ■ ACKNOWLEDGMENTS

This work was financially supported by a project (Project No. JPNP14004, Grant Number: 24018730), commissioned by the New Energy and Industrial Technology Development Organization (NEDO). This work was also partly supported by CREST-Nanomechanics: Elucidation of macroscale mechanical properties based on understanding nanoscale dynamics for innovative mechanical materials (Grant Number: JPMJCR2194) from the Japan Science and Technology Agency (JST). K.M. also gratefully acknowledges the Iketani Science and Technology Foundation. The synchrotron radiation experiments for XAFS measurements were performed at the BL01B1 beamline in SPring-8 with the approval from JASRI (2024B1566 and 2025A1703).

## ■ REFERENCES

(1) Rosen, M. A.; Koohi-Fayegh, S. The Prospects for Hydrogen as an Energy Carrier: An Overview of Hydrogen Energy and Hydrogen Energy Systems. *Energy, Ecol. Environ.* **2016**, *1*, 10−29.

(2) Lim, K. H.; Yue, Y.; Bella, N.; Gao, X.; Zhang, T.; Hu, F.; Das, S.; Kawi, S. Sustainable Hydrogen and Ammonia Technologies with Nonthermal Plasma Catalysis: Mechanistic Insights and Technoeconomic Analysis. *ACS Sustainable Chem. Eng.* **2023**, *11*, 4903−4933.

(3) Li, X.; Shen, P.; Han, X.; Wang, Y.; Zhu, Y.; Wu, Z. Dehydrogenation Mechanisms of Liquid Organic Hydrogen Carriers over Pt, Pd, Rh, and Ni Surfaces: Cyclohexane as a Model Compound. *Appl. Surf. Sci.* **2021**, *543*, No. 148769.

(4) Luo, Y.; Yang, Q.; Nie, W.; Yao, Q.; Zhang, Z.; Lu, Z. H. Anchoring IrPdAu Nanoparticles on $NH_2$-SBA-15 for Fast Hydrogen Production from Formic Acid at Roo Temperature. *ACS Appl. Mater. Interfaces* **2020**, *12*, 8082−8090.

(5) Surkatti, R.; Ewis, D.; Konnova, M. E.; El-Naas, M. H.; Abdellatif, Y.; Alrebei, O. F.; Amhamed, A. Comprehensive Insights into Sustainable Circular Liquid Hydrogen Carriers: Analysis of Technologies and Their Role in Energy Transition. *J. Environ. Chem. Eng.* **2025**, *13*, No. 118197.

(6) Kojima, Y. Hydrogen Storage Materials for Hydrogen and Energy Carriers. *Int. J. Hydrogen Energy* **2019**, *44*, 18179−18192.

(7) Meng, L.; Tsuru, T. Hydrogen Production from Energy Carriers by Silica-Based Catalytic Membrane Reactors. *Catal. Today* **2016**, *268*, 3−11.

(8) Zhu, Q. L.; Xu, Q. Liquid Organic and Inorganic Chemical Hydrides for High-Capacity Hydrogen Storage. *Energy Environ. Sci.* **2015**, *8*, 478−512.

(9) Zhao, X.; Xu, D.; Liu, K.; Dai, P.; Gao, J. Remarkable Enhancement of PdAg/RGO Catalyst Activity for Formic Acid Dehydrogenation by Facile Boron-Doping through $NaBH_4$ Reduction. *Appl. Surf. Sci.* **2020**, *512*, No. 145746.

(10) Zhong, H.; Iguchi, M.; Chatterjee, M.; Himeda, Y.; Xu, Q.; Kawanami, H. Formic Acid-Based Liquid Organic Hydrogen Carrier System with Heterogeneous Catalysts. *Adv. Sustainable Syst.* **2018**, *2*, No. 1700161.

(11) Lee, J. H.; Ryu, J.; Kim, J. Y.; Nam, S. W.; Han, J. H.; Lim, T. H.; Gautam, S.; Chae, K. H.; Yoon, C. W. Carbon Dioxide Mediated, Reversible Chemical Hydrogen Storage Using a Pd Nanocatalyst Supported on Mesoporous Graphitic Carbon Nitride. *J. Mater. Chem. A* **2014**, *2*, 9490−9495.

(12) Mori, K.; Fujita, T.; Yamashita, H. Boosting the Activity of PdAg Alloy Nanoparticles during $H_2$ Production from Formic Acid Induced by $CrO_x$ as an Inorganic Interface Modifier. *EES Catal.* **2023**, *1*, 84−93.

(13) Huang, Y.; Zhou, X.; Yin, M.; Liu, C.; Xing, W. Novel PdAu@Au/C Core-Shell Catalyst: Superior Activity and Selectivity in Formic Acid Decomposition for Hydrogen Generation. *Chem. Mater.* **2010**, *22*, 5122−5128.

(14) Qin, Y. L.; Wang, J.; Meng, F. Z.; Wang, L. M.; Zhang, X. B. Efficient PdNi and PdNi@Pd-Catalyzed Hydrogen Generation via Formic Acid Decomposition at Room Temperature. *Chem. Commun.* **2013**, *49*, 10028−10030.

(15) Zou, L.; Zhang, Q.; Huang, Y.; Luo, X.; Liang, Z. Highly Efficient Hydrogen Generation from a Formic Acid/Triethanolamine System Using a Pd-Based Catalyst and Correlation for Apparent Activation Energy Estimation. *Ind. Eng. Chem. Res.* **2019**, *58*, 22984−22995.

(16) Moret, S.; Dyson, P. J.; Laurenczy, G. Direct Synthesis of Formic Acid from Carbon Dioxide by Hydrogenation in Acidic Media. *Nat. Commun.* **2014**, *5*, No. 4017.

(17) Sivanesan, D.; Song, K. H.; Jeong, S. K.; Kim, H. J. Hydrogenation of $CO_2$ to Formate Using a Tripodal-Based Nickel Catalyst under Basic Conditions. *Catal. Commun.* **2019**, *120*, 66−71.

(18) Mori, K.; Sano, T.; Kobayashi, H.; Yamashita, H. Surface Engineering of a Supported PdAg Catalyst for Hydrogenation of $CO_2$ to Formic Acid: Elucidating the Active Pd Atoms in Alloy Nanoparticles. *J. Am. Chem. Soc.* **2018**, *140*, 8902−8909.

(19) Mori, K.; Shinogi, J.; Shimada, Y.; Yamashita, H. Heterogeneous Tandem Catalysis Strategy for Additive-Free $CO_2$ Hydrogenation into Formic Acid in Water: Crystal Plane Effect of $Co_3O_4$ Cocatalyst. *ACS Catal.* **2024**, *14*, 18861−18871.

(20) Nankya, R.; Elgazzar, A.; Zhu, P.; Chen, F. Y.; Wang, H. Catalyst Design and Reactor Engineering for Electrochemical $CO_2$ Reduction to Formate and Formic Acid. *Mater. Today* **2024**, *76*, 94−109.

(21) Tran, D. S.; Vu, N. N.; Nemamcha, H. E.; Boisvert, C.; Legrand, U.; Fink, A. G.; Navarro-Pardo, F.; Dinh, C. T.; Nguyen-Tri, P. Design of Electrocatalysts and Electrodes for $CO_2$ Electroreduction to Formic Acid and Formate. *Coord. Chem. Rev.* **2025**, *524*, No. 216322.

(22) Ewis, D.; Arsalan, M.; Khaled, M.; Pant, D.; Ba-Abbad, M. M.; Amhamed, A.; El-Naas, M. H. Electrochemical Reduction of $CO_2$ into Formate/Formic Acid: A Review of Cell Design and Operation. *Sep. Purif. Technol.* **2023**, *316*, No. 123811.

(23) Dong, D.; Zhu, J.; Liu, M.; Yan, X.; Lu, B.; Zhou, K. Improving Steam Methane Reforming Efficiency via Hierarchical Structure in Additively Manufactured Ni-Based Self-Catalytic Reactors. *Materials* **2025**, *18*, No. 1350.

(24) Chen, L.; Zhou, S.; Li, M.; Mo, F.; Yu, S.; Wei, J. Catalytic Materials by 3D Printing: A Mini Review. *Catalysts* **2022**, *12*, No. 1081.

(25) Zhao, X.; Karakaya, C.; Qian, M.; Zou, R.; Zhang, W.; Lu, Z.; Maiti, D.; Samanta, A.; Wan, W.; Liu, X.; Tiplea, A.; Li, Y.; Cui, S.;

Wang, C.; Lei, H.; Bankston, S.; Yilmaz, S.; Chen, J. G.; Ozcan, S. 3D Printing Synthesis of Catalysts. *Mater. Today Sustainability* **2024**, *26*, No. 100746.
(26) Wei, Q.; Li, H.; Liu, G.; He, Y.; Wang, Y.; Tan, Y. E.; Wang, D.; Peng, X.; Yang, G.; Tsubaki, N. Metal 3D Printing Technology for Functional Integration of Catalytic System. *Nat. Commun.* **2020**, *11*, No. 4098.
(27) Mori, K.; Fujita, T.; Hata, H.; Kim, H.; Nakano, T.; Yamashita, H. Surface Chemical Engineering of a Metal 3D-Printed Flow Reactor Using a Metal − Organic Framework for Liquid-Phase Catalytic $H_2$ Production from Hydrogen Storage Materials. *ACS Appl. Mater. Interfaces* **2023**, *15*, 51079−51088.
(28) Wang, C.; Peng, X.; He, Y.; Fan, J.; Lin, X.; Jiang, L.; Tsubaki, N. Metal 3D Printed Nickel-Based Self-Catalytic Reactor for $CO_x$ Methanation. *ChemCatChem* **2022**, *14*, No. e202101581.
(29) Browne, M. P.; Redondo, E.; Pumera, M. 3D Printing for Electrochemical Energy Applications. *Chem. Rev.* **2020**, *120*, 2783−2810.
(30) Xu, X.; Tan, Y. H.; Ding, J.; Guan, C. 3D Printing of Next-Generation Electrochemical Energy Storage Devices: From Multiscale to Multimaterial. *Energy Environ. Mater.* **2022**, *5*, 427−438.
(31) Buchbinder, D.; Schleifenbaum, H.; Heidrich, S.; Meiners, W.; Bültmann, J. High Power Selective Laser Melting (HP SLM) of Aluminum Parts. *Phys. Procedia* **2011**, *12*, 271−278.
(32) Kim, H. J.; Mori, K.; Nakano, T.; Yamashita, H. Advances in Metal 3D Printing Technology for Tailored Self-Catalytic Reactor Design. *ChemCatChem* **2024**, *16*, 3−8.
(33) Kim, H. J.; Mori, K.; Nakano, T.; Yamashita, H. Rational Design of Stainless Steel Self-Catalytic Reactors for $CO_2$ Methanation: Extending from Metal Powder to 3D-Printed Reactors. *Catal. Sci. Technol.* **2025**, *15*, 669−672.
(34) Du, Q.; Bao, S.; Wang, K.; Sheng, Z.; Li, C.; Wu, B.; Liu, K.; Gao, X.; Mao, J.; Zhao, T. S.; Zhang, J. Recent Advances in 3D Printing of Tailored Catalysts for Heterogeneous Thermocatalytic Reactions. *Fuel* **2026**, *405*, No. 136554.
(35) Kim, H. J.; Mori, K.; Ichikawa, S.; Nakano, T.; Yamashita, H. Layered $Na_2Ti_3O_7$-Supported Ru Catalyst for Ambient $CO_2$ Methanation. *Nat. Commun.* **2025**, *16* (1), No. 2697.
(36) Ye, R.; Ding, J.; Reina, T. R.; Duyar, M. S.; Li, H.; Luo, W.; Zhang, R.; Fan, M.; Feng, G.; S, J.; L, J. Design of Catalysts for Selective $CO_2$ Hydrogenation. *Nat. Synth.* **2025**, *4*, 288−302.
(37) Ye, R. P.; Ding, J.; Gong, W.; Argyle, M. D.; Zhong, Q.; Wang, Y.; Russell, C. K.; Xu, Z.; Russell, A. G.; Li, Q.; Fan, M.; Yao, Y. G. $CO_2$ Hydrogenation to High-Value Products via Heterogeneous Catalysis. *Nat. Commun.* **2019**, *10*, No. 5698.
(38) Kim, H. J.; Mori, K.; Nakano, T.; Yamashita, H. Robust Self-Catalytic Reactor for $CO_2$ Methanation Fabricated by Metal 3D Printing and Selective Electrochemical Dissolution. *Adv. Funct. Mater.* **2023**, *33* (41), No. 2303994.
(39) Liverani, E.; Toschi, S.; Ceschini, L.; Fortunato, A. Effect of Selective Laser Melting (SLM) Process Parameters on Microstructure and Mechanical Properties of 316L Austenitic Stainless Steel. *J. Mater. Process. Technol.* **2017**, *249*, 255−263.
(40) Salman, O. O.; Brenne, F.; Niendorf, T.; Eckert, J.; Prashanth, K. G.; He, T.; Scudino, S. Impact of the Scanning Strategy on the Mechanical Behavior of 316L Steel Synthesized by Selective Laser Melting. *J. Manuf. Process.* **2019**, *45*, 255−261.
(41) Thijs, L.; Montero Sistiaga, M. L.; Wauthle, R.; Xie, Q.; Kruth, J. P.; Van Humbeeck, J. Strong Morphological and Crystallographic Texture and Resulting Yield Strength Anisotropy in Selective Laser Melted Tantalum. *Acta Mater.* **2013**, *61*, 4657−4668.
(42) Feist, T. P.; Davies, P. K. The Soft Chemical Synthesis of $TiO_2$ (B) from Layered Titanates. *J. Solid State Chem.* **1992**, *101*, 275−295.
(43) An, Y.; Wang, D.; Wu, C. Ion-Exchange between $Na_2Ti_3O_7$ and $H_2Ti_3O_7$ Nanosheets at Different PH Levels: An Experimental and First-Principles Study. *Phys. E* **2014**, *60*, 210−213.
(44) Bathena, T.; Phung, T.; Svadlenak, S. R.; Liu, Y.; Grabow, L. C.; Goulas, K. A. Oxygenate Reactions over PdCu and PdAg Catalysts: Distinguishing Electronic and Geometric Effects on Reactivity and Selectivity. *ACS Catal.* **2022**, *12*, 5766−5775.
(45) Zhang, J.; Fan, L.; Zhao, F.; Fu, Y.; Lu, J. Q.; Zhang, Z.; Teng, B.; Huang, W. Zinc Oxide Morphology-Dependent Pd/ZnO Catalysis in Base-Free $CO_2$ Hydrogenation into Formic Acid. *ChemCatChem.* **2020**, *12*, 5540−5547.
(46) Zhang, Z.; Zhang, L.; Yao, S.; Song, X.; Huang, W.; Hülsey, M. J.; Yan, N. Support-Dependent Rate-Determining Step of $CO_2$ Hydrogenation to Formic Acid on Metal Oxide Supported Pd Catalysts. *J. Catal.* **2019**, *376*, 57−67.
(47) Masuda, S.; Mori, K.; Futamura, Y.; Yamashita, H. PdAg Nanoparticles Supported on Functionalized Mesoporous Carbon: Promotional Effect of Surface Amine Groups in Reversible Hydrogen Delivery/Storage Mediated by Formic Acid/$CO_2$. *ACS Catal.* **2018**, *8*, 2277−2285.
(48) He, C. S.; Gong, L.; Zhang, J.; He, P. P.; Mu, Y. Highly Selective Hydrogenation of $CO_2$ into Formic Acid on a Nano-Ni Catalyst at Ambient Temperature: Process, Mechanisms and Catalyst Stability. *J. CO2 Util.* **2017**, *19*, 157−164.
(49) Jin, C.; Cheng, L.; Feng, G.; Ye, R.; Lu, Z. H.; Zhang, R.; Yu, X. Adsorption of Transition-Metal Clusters on Graphene and N-Doped Graphene: A DFT Study. *Langmuir* **2022**, *38*, 3694−3710.
(50) Wadsley, A. D.; Mumme, W. G. The Crystal Structure of $Na_2Ti_7O_{15}$, and an Ordered Intergrowth of $Na_2Ti_6O_{13}$ and '$Na_2Ti_8O_{17}$'. *Acta Crystallogr., Sect. B* **1968**, *24*, 392−396.
(51) Zhang, X.; Zhao, Q.; Cai, Z.; Pan, J. Effects of Magnetic Field on the Residual Stress and Structural Defects of Ti-6Al-4V. *Metals (Basel).* **2020**, *10*, No. 141.
(52) Lee, J. R.; Lee, M. S.; Yeon, S. M.; Yoon, J.; Lee, H.; Jun, T. S. Unravelling Anisotropic Deformation Behaviour of Ti-6Al-4V ELI Fabricated by Powder Bed Fusion Additive Manufacturing. *Mater. Charact.* **2023**, *202*, No. 113017.
(53) Fujiyama, K.; Mori, K.; Kaneko, D.; Kimachi, H.; Saito, T.; Ishii, R.; Hino, T. Creep Damage Assessment of 10Cr-1Mo-1W-VNbN Steel Forging through EBSD Observation. *Int. J. Pressure Vessels Piping* **2009**, *86*, 570−577.
(54) Zhang, K.; Liu, X.; Fan, P.; Zhu, L.; Wang, K.; Wang, L.; Zhao, C. Characterization of Geometrically Necessary Dislocation Evolution during Creep of P91 Steel Using Electron Backscatter Diffraction. *Mater. Charact.* **2023**, *195*, No. 112501.
(55) Chatterjee, S.; Bhattacharyya, S.; Khushalani, D.; Ayyub, P. Hydrothermally Synthesized Aligned Arrays of Self-Assembled Multiwalled Hydrogen Titanate Nanotubes. *Cryst. Growth Des.* **2010**, *10*, 1215−1220.


https://doi.org/10.1021/acsaem.6c00086
*ACS Appl. Energy Mater.* XXXX, XXX, XXX−XXX